Inspiratory rhythmogenic activity is burst-independent and opioid-sensitive

Xiaolu Sun[1*], Carolina Thörn Pérez[1*], Nagaraj Halemani D[2], Xuesi M. Shao[1], Morgan Greenwood[3], Sarah Heath[1], Jack L. Feldman[1], and Kaiwen Kam[2,†]

[1]Department of Neurobiology, David Geffen School of Medicine at UCLA, Los Angeles, CA 90095, USA
[2]Department of Cell Biology and Anatomy, Chicago Medical School, Rosalind Franklin University of Medicine and Science, North Chicago, IL 60064, USA
[3]RFUMS/DePaul Research Internship Program, Rosalind Franklin University of Medicine and Science, North Chicago, IL 60064, USA

*Equal contribution

[†]Correspondence:
Kaiwen Kam, Ph.D.
Department of Cell Biology and Anatomy
Chicago Medical School
Rosalind Franklin University of Medicine and Science
3333 Green Bay Rd.
North Chicago, IL 60064-3095, USA
Email: kaiwen.kam@rosalindfranklin.edu
Phone: (847) 578-8630
Fax: (847) 578-3253

Summary

How mammalian neural circuits generate rhythmic activity in motor behaviors, such as breathing, walking, and chewing, remains elusive. For breathing, rhythm generation can be localized to a brainstem nucleus called the preBötzinger Complex (preBötC). Rhythmic preBötC population activity consists of small amplitude burstlets, which we hypothesize are rhythmogenic, and larger inspiratory bursts, which drive motoneuronal activity. If burstlets are rhythmogenic, opioids, analgesics that can cause profound respiratory depression, should similarly reduce burstlet frequency. In conditions where burstlets were separated from bursts in medullary slices from neonatal mice, the μ-opioid receptor (μOR) agonist DAMGO decreased burstlet frequency. DAMGO-mediated depression was abolished by genetic deletion of μORs in a glutamatergic preBötC subpopulation and was reduced by Substance P, but not blockade of inhibitory synaptic transmission. Our findings suggest that rhythmogenesis need not rely on strong bursts of activity associated with motor output and point to strategies for ameliorating opioid-induced depression of breathing.

Keywords: opioids, breathing, rhythm generation, central pattern generator

Introduction

Rhythmic motor behaviors in mammals, such as breathing, walking, and chewing, are controlled by neural circuits that determine the period of the movement and shape the pattern of motor activity. Despite the apparent simplicity of the computation, the mechanisms underlying rhythmogenesis in these circuits are unknown. Generation of breathing rhythm is localized to a compact nucleus in the ventrolateral medulla, the preBötzinger Complex (preBötC; Smith et al., 1991). In particular, two overlapping subpopulations of glutamatergic preBötC neurons, those expressing the neurokinin-1 receptor (NK1R) and those derived from progenitors that express the transcription factor Dbx1 (Dbx1^{+}), are necessary for inspiratory rhythmogenesis (Bouvier et al., 2010; Gray et al., 2010; Gray et al., 2001).

Until recently, rhythmic bursts of preBötC population activity were considered unitary events that determined both the timing and pattern of periodic inspiratory movements. However, we recently showed that these preBötC bursts consist of two separable components: i) large amplitude inspiratory bursts that are transmitted via premotoneurons to inspiratory motoneurons to activate muscles that produce inspiratory airflow; and ii) low amplitude burstlets that appear as preinspiratory activity when preceding these bursts and are not normally seen in motor nerve or muscle activity (Kam et al., 2013a). Because preBötC rhythmic activity can consist solely of burstlets that do not produce motoneuronal output, we hypothesize that burstlets are rhythmogenic (Kam et al., 2013a). A strong prediction of this hypothesis is that manipulations that affect inspiratory burst frequency should have similar effects on preBötC burstlet frequency.

To test this prediction, we examined the effects of opioids, analgesics that depress breathing at high doses, on bursts and burstlets and tested opioidergic interactions with other neurotransmitters and neuromodulators that affect preBötC neuronal excitability. We bath-applied [D-Ala^{2},N-MePhe^{4},Gly-ol^{5}]-enkephalin (DAMGO), a potent synthetic μ-opioid receptor (μOR) agonist, in conditions of low excitability *in vitro* when burstlets appeared at times bursts would have been expected or when preBötC rhythmic activity consisted solely of burstlets. We measured the frequency of inspiratory-related preBötC population activity, i.e., the intervals

45 between successive bursts or burstlets, to assay opioidergic effects on rhythmogenesis and
46 calculated the fraction of rhythmic preBötC events that were burstlets to assay changes in the
47 pattern-generating threshold mechanism that converts burstlets into bursts. We conclude that
48 DAMGO depresses inspiratory frequency by acting on burstlet producing preBötC Dbx1$^+$
49 neurons. These data are consistent with our hypothesis of distinct rhythm and pattern
50 generating mechanisms within the preBötC, with rhythmogenesis being mediated by burstlets
51 and a separable burst-generating mechanism governing patterned preBötC output. Our results
52 also inform potential approaches for combating opioid-induced depression of breathing.

53 **Results**

54 **DAMGO slows preBötC rhythmic activity without affecting burstlet fraction.**

55 Systemic administration of opioids slows breathing *in vivo* and *in vitro* (Boom et al., 2012; Gray
56 et al., 1999). We investigated how preBötC burstlets and bursts mediate these opioidergic
57 effects in neonatal mouse tissue slices that contain the preBötC and the hypoglossal motor
58 nucleus and nerve (XII) and generate a physiologically relevant motor output, i.e., inspiratory-
59 related rhythmic activity. Under baseline conditions in artificial cerebrospinal fluid (ACSF)
60 containing 9 mM K^+ and 1.5 mM Ca^{2+} ("9/1.5"), preBötC population activity and XII activity
61 consisted primarily of coincident, large amplitude rhythmic bursts (Fig. 1A; Smith et al., 1991).
62 Subsaturating concentrations of DAMGO caused a dose-dependent decrease in the frequency
63 (*f*) of rhythmic preBötC and XII bursts (Fig. 1A-C). 10 nM DAMGO significantly decreased
64 preBötC *f* from 0.22 ± 0.05 Hz to 0.13 ± 0.04 Hz (p=0.01, n=6; Fig. 1C). 30 nM DAMGO
65 application further decreased preBötC *f* to 0.07 ± 0.04 Hz (p=0.0001, n=6; Fig. 1C), and 100 nM
66 DAMGO led to complete cessation of XII activity and, in some cases, also blocked all preBötC
67 activity (Fig. 1B).

68 We previously showed that changes in XII *f* induced by decreases in extracellular K^+ could be
69 caused by a reversion of preBötC bursts to preBötC burstlets (Kam et al., 2013a). This was not
70 the case for the effects of DAMGO on *f*, as the fraction of total preBötC events that were
71 burstlets (burstlet fraction), which was very low in control conditions (0.14 ± 0.14), was not

72 significantly different from that in the presence of 30 or 100 nM DAMGO (p=0.8, n=6; Fig. 1A,
73 C). Moreover, the amplitude of preBötC bursts (0.60 ± 0.10 a.u.) was not significantly different
74 between control conditions without DAMGO and when 10 nM (0.61 ± 0.13 a.u.) or 30 nM
75 DAMGO (0.56 ± 0.19 a.u.) was added to the bath (p=0.8, n=6).

76 To determine whether DAMGO could affect the conversion of burstlets into bursts when the
77 preBötC was operating in a different dynamic mode, we decreased ACSF K^+ and Ca^{2+}
78 concentrations (Kam et al., 2013a). In 3 mM K^+ and 1 mM Ca^{2+} ("3/1"), preBötC activity was a
79 mixed pattern of burstlets and bursts (Fig. 1D, upper traces). While the burstlet fraction under
80 these conditions (0.58 ± 0.26) was significantly higher than that in 9/1.5 ACSF (0.14 ± 0.14;
81 p=0.003, n= 6 for 9/1.5, n=7 for 3/1), preBötC *f* was similar (0.23 ± 0.10 Hz in 3/1 vs. 0.22 ± 0.05
82 Hz in 9/1.5; p=0.8, n= 6 for 9/1.5, n=7 for 3/1; Fig. 1C, F). XII *f* in 3/1 ACSF (0.08 ± 0.05 Hz), on
83 the other hand, was significantly lower than XII *f* in 9/1.5 ACSF (0.2 ± 0.06 Hz; p=0.002, n= 6 for
84 9/1.5, n=7 for 3/1; Fig. 1B, E), a consequence of the increased fraction of preBötC burstlets that
85 were not transmitted to XII output.

86 In 3/1 ACSF, DAMGO decreased preBötC *f* in a dose-dependent manner, similar to its effects in
87 9/1.5 ACSF. Addition of 30 nM DAMGO significantly reduced preBötC *f* from 0.22 ± 0.1 Hz to
88 0.04 ± 0.04 Hz (p=0.001, n=7; Fig. 1D-F). This reduction was not significantly different from the
89 effects of 30 nM DAMGO in 9/1.5 ACSF (p=0.2, n=6 for 9/1.5, n=7 for 3/1; Fig. 1C, F). Higher
90 concentrations of DAMGO (≥100 nM) frequently blocked all preBötC population activity.
91 Burstlet and burst amplitudes in 3/1 ACSF (burstlet: 0.38 ± 0.05 a.u.; burst: 0.73 ± 0.08 a.u.) did
92 not change significantly when 10 nM DAMGO (burstlet: 0.36 ± 0.04 a.u.; burst: 0.78 ± 0.10 a.u.)
93 or 30 nM DAMGO (burstlet: 0.34 ± 0.11 a.u.; burst: 0.65 ± 0.21 a.u.) was bath-applied (burstlet:
94 p=0.7, burst: p=0.3, n=7), and the burstlet fraction was again unaffected by DAMGO (p=1.0,
95 n=7; Fig. 1F).

96 To determine whether opioids specifically affected rhythmogenic activity independent of burst
97 production, we isolated burstlets using low concentrations of Cd^{2+} (6-25 µM; Kam et al., 2013a),
98 which significantly increased the burstlet fraction from 0.42 ± 0.30 to 0.78 ± 0.20 (p=0.02, n=8)
99 without significantly changing preBötC *f* or amplitude (*f*: p=0.7, amplitude: p=0.06, n=8; Fig. 2A,

100 B). The decreases in excitability and synaptic efficacy caused by Cd^{2+} (Kam et al., 2013a; Lu et
101 al., 2007) resulted in an increased sensitivity to DAMGO. Bath application of 1 nM DAMGO on
102 this burstlet only rhythm was sufficient to abolish preBötC rhythmic activity completely in 7 of 8
103 slices. Concentrations of DAMGO below that causing rhythmic cessation (0.01-10 nM) slowed
104 preBötC *f* significantly from 0.28 ± 0.09 Hz to 0.18 ± 0.07 Hz (p=0.001, n=8; Fig. 2A, B). This
105 relative decrease in preBötC *f* (0.66 ± 0.16) was not significantly different from the effect of 10
106 nM DAMGO on preBötC *f* in 3/1 ACSF with no Cd^{2+} (0.63 ± 0.16; p=0.8, n=5 for 3/1, n=8 for
107 Cd^{2+}). However, burstlet amplitudes in the presence of both Cd^{2+} and DAMGO (0.29 ± 0.08)
108 were significantly reduced compared to Cd^{2+} alone (0.35 ± 0.09; p=0.003, n=8; Fig. 2A, B).

109 Depression of preBötC burstlet *f* by μOR activation points to DAMGO modulating preBötC
110 rhythmogenic mechanisms. We previously hypothesized that the emergent rhythmogenic
111 processes that produce burstlets manifested as the latency in ectopic burst initiation following
112 targeted excitation of 4-9 preBötC inspiratory neurons, whose molecular identity was
113 unspecified (Kam et al., 2013b). Here, in slices from $Dbx1^{+}$ reporter (*Dbx1*^{cre};*Rosa26*^{tdTomato})
114 mice, we targeted preBötC $Dbx1^{+}$ neurons for holographic photostimulation to determine if
115 opioids also modulate this rhythmogenesis-related process (Fig. 2C-F). In control 9/1.5 ACSF,
116 ectopic bursts were reliably elicited when 5-10 $Dbx1^{+}$ neurons were targeted (probability of
117 success: 0.86 ± 0.08, n=6; Fig. 2D). When a set of neurons that reliably resulted in bursts in
118 response to photostimulation in control conditions were then excited in 30 nM DAMGO, the
119 probability of eliciting a burst was reduced to 0.48 ± 0.25 (n=4; Fig. 2D, E). In 100 nM DAMGO,
120 the success rate decreased significantly as stimulation of the threshold set that had previously
121 reliably triggered bursts was further compromised and, in some cases, failed to trigger a single
122 burst (p=0.006, n=6; Fig. 2D, E). In 200 nM DAMGO, stimulation was unsuccessful at eliciting
123 bursts (p=0.0003, n=6; Fig. 2E). Importantly, the latency between laser stimulation and burst
124 initiation in the cases when bursts were triggered in DAMGO (157 ± 22 ms) was significantly
125 increased compared to that in baseline conditions (105 ± 24 ms; p=0.002, n=5; Fig. 2F).

126 **μOR-expressing $Dbx1^{+}$ neurons mediate the rhythmogenic effects of opioids.**

127 Which preBötC neurons does DAMGO target to depress inspiratory rhythm? We hypothesized

128 that DAMGO was acting on preBötC Dbx1^{+} neurons, which are essential for respiratory rhythm
129 generation (Bouvier et al., 2010; Gray et al., 2010; Wang et al., 2014) and contain μOR mRNA
130 (Hayes et al., 2017). We first sought to determine whether these neurons express μOR protein
131 using immunohistochemistry. In *Dbx1^{Cre};Rosa26^{tdTomato}* mice, μOR protein expression
132 overlapped with the spatial distribution of tdTomato-expressing Dbx1^{+} neurons in preBötC and
133 the adjacent intermediate band of the reticular formation (IRt; Fig. 3A) and was localized to
134 individual preBötC Dbx1^{+} neurons (Fig. 3B-C).

135 To test whether μORs in Dbx1^{+} neurons mediated DAMGO inhibition, we used a
136 *Dbx1^{Cre};Oprm1$^{fl/fl}$* mouse line (Weibel et al., 2013), in which μORs are genetically deleted in
137 Dbx1^{+} neurons. We first examined whether preBötC μOR expression was knocked down in P2
138 *Dbx1^{Cre};Oprm1$^{fl/fl}$* mice compared to their littermate controls (Fig. 3D-I). *Dbx1* is not expressed
139 postnatally (Bouvier et al., 2010; Gray et al., 2010), and NK1R protein is predominantly found in
140 neuronal processes (Tan et al., 2010) while NK1R mRNA is sparsely expressed in somata (Fig.
141 S1). We therefore localized preBötC using tachykinin precursor peptide (TAC1) expression,
142 which colocalizes with NK1R, ventral to nucleus ambiguus (NA) as a marker for preBötC (Fig. S1;
143 Hayes et al., 2017). To measure μOR and TAC1 expression, we performed fluorescence *in situ*
144 hybridization, which avoids the non-specific labeling that may occur with some μOR antibodies
145 (Schmidt et al., 2013) and allows localization of TAC1 expression to somata (Fig. S1). Abundant
146 (>15 puncta) TAC1 mRNA was found in larger neurons confined to the preBötC (somatic
147 diameter: 27.08 ± 4.3 μm, n=121). Choline acetyl transferase (ChAT) mRNA probes were used to
148 mark NA. In *Dbx1$^{+/+}$; Oprm1$^{fl/fl}$* control mice, μOR mRNA puncta colocalized with TAC1 and NK1R
149 mRNA in the preBötC (Figs. 3D-F, S1), recapitulating the immunohistochemical distribution of
150 Dbx1^{+} neurons in the Dbx1^{+} reporter mice (Fig. 3A-C). Compared with μOR expression in
151 *Dbx1$^{+/+}$; Oprm1$^{fl/fl}$* mice (Fig. 3D-F), μOR expression in *Dbx1^{Cre}; Oprm1$^{fl/fl}$* mice was reduced in
152 regions where Dbx1^{+} neurons are normally found (Fig. 3D, G) and significantly reduced in TAC1
153 positive preBötC neurons (p=0.01, *Dbx1$^{+/+}$; Oprm1$^{fl/fl}$*: H-score = 139.07 ± 39.33, n = 5; *Dbx1^{Cre};*
154 *Oprm1$^{fl/fl}$*: H-score= 47.98 ± 19.77, n=3; Fig. 3G-I).

155 Having confirmed a decrease in μOR expression in preBötC in *Dbx1^{Cre}; Oprm1$^{fl/fl}$* mice, we

156 determined whether the functional effects of DAMGO on preBötC rhythm were similarly
157 affected. In rhythmic tissue slices from *Dbx1*^{Cre}; *Oprm1*$^{fl/fl}$ mice bathed in 9/1.5 ACSF, 100 nM
158 DAMGO had little effect on preBötC *f* (p=0.2, n=9; Figs. 3J, S2). In contrast, bath-applied
159 DAMGO in *Dbx1*$^{+/+}$; *Oprm1*$^{fl/fl}$ cre-negative littermates reduced preBötC *f* significantly (p=0.01,
160 n=6; Fig. 3J).

161 **DAMGO-mediated depression is diminished by Substance P, but not blockade of inhibitory**
162 **synaptic transmission.**

163 The coexpression of μOR and NK1R in preBötC Dbx1^{+} neurons raises the possibility that NK1R
164 activation, which increases respiratory frequency in wild type rodents (Gray et al., 1999; Yeh et
165 al., 2017), could be effective in reducing the depressant effects of DAMGO. When applied
166 together in 3/1 ACSF, 30 nM DAMGO was much less effective in reducing rhythmic activity in
167 the presence of the NK1R agonist SP (500 nM), and preBötC *f* was not significantly different
168 from that in control 3/1 ACSF conditions, i.e., in the absence of SP and DAMGO (p=0.09, n=6;
169 Fig. 4A,C). We next tested whether altering preBötC excitability by blockade of inhibitory
170 synaptic transmission using a cocktail of the $GABA_A$ receptor antagonist picrotoxin and the
171 glycine receptor antagonist strychnine (picrotoxin/strychnine; Del Negro et al., 2009; Ren and
172 Greer, 2006; Shao and Feldman, 1997) would similarly block DAMGO-mediated depression. In
173 contrast to SP, picrotoxin/strychnine (100 μM/1 μM) did not reduce the effects on preBötC *f* of
174 30 nM DAMGO compared to control conditions in either 9/1.5 or 3/1 ACSF (p=0.2, n=6 for
175 9/1.5, n=7 for 3/1, n=13 for picrotoxin/strychnine; Fig. 4B, C). Indeed, preBötC *f* when SP was
176 applied with 30 nM DAMGO was greater than that in 9/1.5 ACSF, with or without
177 picrotoxin/strychnine, or 3/1 ACSF in the presence of DAMGO (p=0.001, n=6 for 9/1.5, n=7 for
178 3/1, n=12 for picrotoxin/strychnine, n=6 for SP; Fig. 4C).

179 Are the differential efficacies of SP and blockade of inhibitory transmission expressed in their
180 effects on baseline rhythmic activity? To determine how SP and blockade of inhibitory
181 transmission affect rhythm and pattern generation, we tested the effects of SP and
182 picrotoxin/strychnine on preBötC activity in 3/1 ACSF without DAMGO. Under these conditions,
183 bath-applied SP (500 nM) significantly reduced the burstlet fraction from 0.47 ± 0.3 to

184 0.10 ± 0.12 (p=0.01, n=6), but, surprisingly, did not affect preBötC *f* (p=0.4, n=6; Fig. 4D, E). In
185 slices from *Dbx1*^{Cre}*; Oprm1*$^{fl/fl}$ mice bathed in 9/1.5 ACSF, we confirmed that 500 nM SP
186 significantly increased preBötC *f* (Fig. S2) and modulated preBötC *f* independent of μORs, which
187 were deleted in Dbx1^{+} neurons in these slices. In 3/1 ACSF, bath-applied picrotoxin/strychnine
188 (100 μM/1 μM) also significantly decreased burstlet fraction (p=0.0001, n=13) and did not alter
189 preBötC *f* significantly (p=0.9, n=13; Fig. 4F, G).

190 **Discussion**

191 Inspiratory rhythm generation must be both robust, to operate almost continuously throughout
192 the lifetime of the animal, and labile, to adapt to changing metabolic and environmental
193 conditions and coordinate with other behaviors. How the preBötC generates rhythm to meet
194 these challenges has thus far defied a thorough understanding. We put forth a hypothesis that
195 respiratory rhythmogenesis is driven not by strong bursts, but by preBötC burstlets (Fig. 4H;
196 Kam et al., 2013a). Burstlets occur when spontaneous firing among preBötC neurons reaches a
197 threshold for synchrony, and the time required for preBötC neurons to assemble and achieve
198 this synchrony (percolation) determines the period of the rhythm (Kam et al., 2013a; S.A. and
199 J.L.F., in preparation).

200 A strong prediction of this hypothesis is that manipulations that depress burst frequency should
201 also slow burstlet frequency. Indeed, we found that DAMGO specifically slowed preBötC *f*
202 without affecting burstlet fraction when the rhythm: i) was composed of mostly bursts; ii) was a
203 mixed pattern of bursts and burstlets; or iii) was mostly (or all) burstlets (Fig. 4H). Additionally,
204 DAMGO prolonged the latency between photostimulation and burst generation when threshold
205 sets of ≤10 neurons were excited. The congruent effects of DAMGO on both burstlet *f* and
206 photostimulation latency: i) is consistent with our hypothesis that both are products of
207 percolation of activity within the preBötC microcircuit, a critical process for rhythmogenesis
208 (Kam et al., 2013a; Kam et al., 2013b), and ii) suggests that DAMGO directly affects
209 rhythmogenic mechanisms.

210 Consistent with our functional studies, we found abundant μOR expression in preBötC Dbx1^{+}

211 neurons that form the core circuitry for inspiratory rhythmogenesis (Wang et al., 2014). We
212 also showed colocalization of μOR with NK1R in some preBötC neurons as well as with a
213 partially overlapping preBötC subpopulation expressing TAC1 that may be one endogenous
214 source of SP (Liu et al., 2004). When μORs were genetically deleted in Dbx1^{+} neurons in *Dbx1*^{Cre};
215 *Oprm1*$^{fl/fl}$ mice, the potent rhythmic slowing effect of DAMGO in slices was no longer present.
216 These data suggest that μORs in preBötC Dbx1^{+} neurons mediate DAMGO inhibition of
217 rhythmicity.

218 How could μOR activation affect the percolation of activity in the preBötC that we hypothesize
219 underlies rhythmogenesis and transform, i.e., slow down, the dynamics of the Dbx1^{+} preBötC
220 network? μORs can be localized postsynaptically on dendrites and cell bodies, where they
221 regulate neuronal excitability and transduce receptor activation to downstream signal
222 transduction pathways; μORs are also found presynaptically on axon terminals where they
223 inhibit neurotransmitter release via activation of K^{+} conductances and/or inhibition of Ca^{2+}
224 conductances (Le Merrer et al., 2009; Mansour et al., 1988; Montandon et al., 2016; Williams et
225 al., 2001). We suggest that DAMGO-mediated hyperpolarization and/or decreases in synaptic
226 probability of release in and among μOR-expressing preBötC Dbx1^{+} neurons reduce
227 spontaneous firing rate, weaken the propagation of action potentials to postsynaptic neurons,
228 and increase the number of inputs required to reach action potential threshold. These effects
229 reduce the moment-to-moment probability that a critical number of neurons will be
230 simultaneously active and prolong the time required for preBötC neurons to increase their
231 firing, achieve synchrony, and generate burstlets (S.A. and J.L.F., in preparation).

232 The pattern-generating mechanism that converts burstlets to bursts may, by analogy, require a
233 higher threshold of activity and synchrony be reached via independently regulated, distinct
234 mechanisms, such as the activation of persistent inward conductances (Picardo et al., 2019).
235 Through this threshold mechanism, SP and blockade of inhibitory synaptic transmission
236 increase, whereas Cd^{2+} decreases, the fraction of preBötC events that are burstlets, without
237 altering frequency of these events (Fig. 4H). Interestingly, the depressant effects of DAMGO
238 were reduced by SP, but not inhibitory blockade. Inhibitory synaptic activity in preBötC is

239 dispensable for generation of breathing rhythm *in vivo* and *in vitro* (Janczewski et al., 2013;
240 Shao and Feldman, 1997) and has variable effects on excitability (Ren and Greer, 2006), which
241 may account for the inability of picrotoxin and strychnine to mitigate DAMGO-induced
242 depression. Alternatively, inhibition may act elsewhere in the microcircuit or upstream of
243 opioidergic signaling pathways within Dbx1$^+$ neurons. While inhibitory blockade specifically
244 affects pattern generation and is unable to rescue DAMGO-mediated depression, NK1R
245 activation is capable of modulating both rhythm and pattern in a state-dependent manner and
246 can mitigate the effects of DAMGO (Fig. 4H), due perhaps to intracellular interactions in
247 preBötC Dbx1$^+$ neurons that coexpress μOR and NK1R.

248 The μOR expression and DAMGO sensitivity of NK1R-expressing neurons are well-documented
249 (Gray et al., 1999; Montandon et al., 2011), and G_s-protein coupled signaling of NK1R opposes
250 the $G_{i/o}$-coupled signaling of μORs (Gray et al., 1999; Johnson et al., 1996). However, the
251 interaction of NK1R and μOR can be complicated. Opioids may inhibit SP release, and SP
252 potentiates the antinociceptive effects of morphine through release of endogenous opioids
253 (Fukazawa et al., 2007; Kream et al., 1993). SP may also act directly on μORs as a weak agonist
254 since naloxone, the μOR antagonist, blocks SP excitation in some neurons (Davies and Dray,
255 1977). Nonetheless, we predict that only neuropeptides and neuromodulators, whose
256 receptors are coexpressed with μORs in rhythmogenic preBötC neurons, like NK1Rs, are able to
257 modulate μOR signaling intracellularly to mitigate DAMGO-mediated depression.

258 The interaction between excitatory neuromodulatory systems with opiates in respiratory neural
259 circuits is relevant for addressing the depressive effects of opiates on breathing. Opioids are the
260 most commonly prescribed drugs for severe acute and chronic pain and play an important role
261 in palliative care. However, with a high potential for addiction, opiate overprescription and
262 abuse has created a pressing public health crisis that affects millions. Morbidity and mortality
263 from opioid addiction and overdose is largely a result of opioid-induced depression of breathing
264 (Jaffe & Martin, 1990). Opiates given systemically will act on opioid receptors throughout the
265 nervous system (Kibaly et al., 2019), and μORs are expressed in various brain structures
266 regulating breathing (Gray et al., 1999; Manzke et al., 2003; Phillips et al., 2012; Pokorski and

267 Lahiri, 1981; Prkic et al., 2012; Zhang et al., 2007; Zhang et al., 2011). While depression of
268 breathing is unlikely to be dependent on actions at a single site (Lalley et al., 2014; Montandon
269 and Horner, 2014; Stucke et al., 2015), our data is consistent with compelling *in vitro* and *in vivo*
270 evidence that the preBötC is the most sensitive site to μOR agonists and that it mediates
271 respiratory frequency depression by opioids (Ballanyi and Ruangkittisakul, 2009; Feldman and
272 Del Negro, 2006; Feldman et al., 2013; Janczewski et al., 2002; Montandon and Horner, 2014;
273 Montandon et al., 2011).

274 In summary, the depressive effect of the μOR agonist DAMGO on preBötC burstlet frequency, in
275 the absence of a change in burstlet fraction, supports a primary role for burstlets in respiratory
276 rhythm generation and is consistent with the hypothesis that rhythm and pattern generating
277 mechanisms within the preBötC are separable. We propose that having distinct mechanisms
278 generating burstlets and bursts provides functional substrates for targeted modulation of the
279 rhythmic timing and/or pattern of breathing by other brain areas and neuromodulators. This
280 organization enables the dynamic temporal and pattern lability characteristic of breathing
281 essential for adaptation to changing metabolic demands and for coordination with other
282 respiratory-related and orofacial behaviors. A better understanding of the mechanisms of μOR
283 actions in respiratory neural circuits has important implications for developing stimulants that
284 excite breathing via non-opioidergic pathways (van der Schier et al., 2014) and drugs that
285 reverse opioid actions on preBötC Dbx1^{+} neurons to maintain breathing without affecting
286 analgesia.

287

288 **Acknowledgements**

289 The authors thank Grace Li for excellent technical work. *Oprm1*$^{fl/fl}$ mice were generously
290 provided by Dr. Wendy Weibel, Dr. Chris Evans, and the Animal Breeding Core (NIDA P50 Center
291 Grant, DA005010). This work was supported by National Institutes of Health grants NS07221,
292 HL135779, and NS097492; and an international postdoctoral grant from the Swedish Research
293 Council (Vetenskapsrådet).

294

Author contributions: X.S., J.L.F., and K.K. designed the research; X.S., C.T.P., N.H., X.M.S., M.G., S.H., and K.K. performed the research; X.S., C.T.P. and K.K. analyzed the data; X.S., C.T.P., J.L.F., and K.K. wrote the paper.

Declaration of Interests

The authors declare no competing interests.

301 **Figure legends**

302 **Figure 1. μOR activation depresses inspiratory frequency without affecting burstlet fraction.**
303 (A) Representative traces of ∫preBötC and ∫XII population activity in 9/1.5 ACSF control (ctrl)
304 and 30 nM DAMGO. Scale bar, 10 s.
305 (B) Representative time course of an experiment where increasing concentrations of DAMGO
306 were bath-applied in 9/1.5 ACSF. Interevent intervals (int.) in preBötC (top) and XII (bottom) are
307 plotted. In this experiment, 100 nM DAMGO led to cessation of rhythm.
308 (C) Average burstlet fraction and preBötC *f* in 9/1.5 ACSF control condition (ctrl) and 10 nM and
309 30 nM DAMGO. Increasing concentrations of DAMGO did not significantly affect burstlet
310 fraction whereas preBötC *f* was significantly lower in 10 nM and 30 nM DAMGO. *, $p < 0.05$,
311 One-way ANOVA, post-hoc Tukey test, n=6.
312 (D) Representative traces of ∫preBötC and ∫XII population activity in 3/1 ACSF control (ctrl) and
313 30 nM DAMGO. Both small amplitude burstlets (•), which did not produce XII activity, and large
314 amplitude bursts, which generated XII bursts, were observed. Scale bar, 10 s.
315 (E) Representative time course of an experiment, where increasing concentrations of DAMGO
316 were bath-applied in 3/1 ACSF. Interevent intervals in preBötC (top) and XII (bottom) are
317 plotted. In this experiment, 100 nM DAMGO led to cessation of XII activity while preBötC
318 rhythm persisted.
319 (F) Average burstlet fraction and *f* in 3/1 ACSF control condition (ctrl) and 10 nM and 30 nM
320 DAMGO. Increasing concentrations of DAMGO did not significantly affect burstlet fraction
321 whereas preBötC *f* was significantly lower in 30 nM DAMGO. *, $p < 0.05$, One-way ANOVA, post-
322 hoc Tukey test, n=7.

323 **Figure 2. DAMGO specifically modulates preBötC rhythmogenesis.**
324 (A) Representative traces of ∫preBötC and ∫XII population activity in 3/1 ACSF control (ctrl), 8
325 μM Cd^{2+}, and 8 μM Cd^{2+} + 10 nM DAMGO. In control conditions (top), rhythmic activity
326 consisted of both burstlets and bursts. After Cd^{2+} application (middle), preBötC bursts were no
327 longer observed, and XII activity was abolished, leaving only a preBötC burstlet rhythm with a *f*

328 similar to control. With addition of DAMGO (bottom), burstlet *f* and amplitude decreased. Scale
329 bar, 5 s.
330 (B) Average burstlet fraction, preBötC *f*, and burstlet amplitude (amp.) in 3/1 ACSF control
331 conditions (ctrl), 6-25 µM Cd^{2+}, and 6-25 µM Cd^{2+} + 0.1-10 nM DAMGO. Addition of Cd^{2+}
332 significantly increased the burstlet fraction while preBötC *f* and burstlet amplitudes were
333 unchanged. Bath application of DAMGO did not alter the burstlet fraction but did significantly
334 decrease preBötC *f* (consisting almost solely of burstlets) and burstlet amplitude. *, $p < 0.05$,
335 One-way ANOVA, post-hoc Tukey test, n=8.
336 (C) Representative image of tdTomato fluorescence in the preBötC of a medullary slice from a
337 *Dbx1*^{cre}*;Rosa26*^{tdTomato} mouse. Dashed circles represent holographic spots over targeted $Dbx1^{+}$
338 neurons. Scale bar, 20 µm.
339 (D) Overlays of representative traces of ∫preBötC from successive laser stimulations of the 8
340 $Dbx1^{+}$ neurons shown in (C) in control 9/1.5 ACSF, 30 nM DAMGO, and 100 nM DAMGO. Arrow
341 represents time of laser stimulation. In control conditions, a failure was seen, but burst
342 initiation was otherwise reliably successful. Bursts were consistently triggered after a ~100 ms
343 latency. In 30 nM DAMGO, failures were more frequent when the same stimulation parameters
344 were used, and the latency between laser stimulation and burst initiation was longer and more
345 variable. In 100 nM DAMGO, bursts were no longer triggered with the same stimulation
346 parameters. Scale bar, 200 ms.
347 (E) Average success rate for burst initiation in control 9/1.5 ACSF (ctrl) conditions and in
348 increasing concentrations of DAMGO using entraining stimuli that elicits >80% success in 9/1.5
349 ACSF. To entrain the rhythm, 5-10 $Dbx1^{+}$ neurons were stimulated 8 - 20 times every 3-6 s.
350 DAMGO produced a dose-dependent decrease in the success rate (stim→burst) for triggering
351 bursts with a significant reduction in success between control and at 100 nM and 200 nM
352 DAMGO. *, $p < 0.05$, One-way ANOVA, post-hoc Tukey test, n=6.
353 (F) Average latency between laser stimulation and burst initiation when bursts were
354 successfully triggered during entraining stimuli was increased in 30 nM DAMGO compared to
355 control 9/1.5 ACSF (ctrl). *, $p<0.05$, Students t-test, n=5.

356 **Figure 3. μORs expressed in Dbx1^{+} neurons mediate DAMGO inhibition of preBötC rhythmic**
357 **activities.**
358 (A) Confocal images of brainstem sections of a *Dbx1^{Cre};Rosa26^{tdTomato}* mouse pup (P2) double-
359 stained with antibodies to ChAT (blue) and μOR (green). Coronal sections showing μOR
360 expression in the preBötC and the Intermediate band of the Reticular Formation (IRt) and
361 colocalization with Dbx1^{+} neurons in the preBötC. Scale bar, 500 μm.
362 (B) Higher magnification of nucleus ambiguus (NA) and preBötC from the boxed region in A.
363 Scale bar, 50 μm.
364 (C) Expanded images of the boxed preBötC region highlighted in B. The arrow shows a preBötC
365 Dbx1^{+} neuron with abundant punctate μOR expression on the cell body. Scale bar, 10 μm.
366 (D) Confocal image of a medullary brainstem section at the level of the preBötC from a control
367 P2 *Dbx1$^{+/+}$; Oprm1$^{fl/fl}$* mouse processed with RNAScope. Probes for μOR (magenta), TAC1
368 (white), and acetylcholine esterase (ChAT; green) were used, and the tissue was counterstained
369 with DAPI (blue). A box marks the location of preBötC. Scale bar, 1 mm.
370 (E) Higher magnification of the boxed preBötC region in D. μOR and TAC1 were highly expressed
371 in this region. Scale bar, 100 μm.
372 (F) Higher magnification images of μOR-expressing neurons with (arrows) and without
373 (arrowhead) TAC1 expression from E. Colocalization of TAC1 and multiple μOR puncta was
374 observed in several neurons as well as abundant μOR puncta in neurons that did not express
375 TAC1. Scale bar, 40 μm.
376 (G) Confocal image of a medullary brainstem section at the level of the preBötC from a P2
377 *Dbx1$^{cre/cre}$; Oprm1$^{fl/fl}$* mouse processed with RNAScope. Probes for μOR (magenta), TAC1
378 (white), and acetylcholine esterase (ChAT; green) were used, and the tissue was counterstained
379 with DAPI (blue). In the preBötC of these mice, the density of μOR puncta was low. A box marks
380 the location of preBötC. Scale bar, 1 mm.
381 (H) Higher magnification of the boxed preBötC region in G. The density of μOR puncta was low,
382 and μOR expression was not associated with TAC1 expression. Scale bar, 100 μm.

383 (I) Higher magnification images of TAC1-expressing neurons from H with few to no μOR puncta
384 (arrows) as well as μOR-expressing neurons without TAC1 expression (arrowhead). Scale bar, 40
385 μm.
386 (J) Average *f* of preBötC activity in control 9/1.5 conditions (ctrl) and 100 nM DAMGO in
387 *Dbx1*^{Cre}; *Oprm1*$^{fl/fl}$ mice (right), where μORs are selectively deleted in Dbx1^{+} neurons, and their
388 *Dbx1*$^{+/+}$;*Oprm1*$^{fl/fl}$ littermate controls with preserved μOR expression (left). Whereas 100 nM
389 DAMGO reduced preBötC *f* significantly in *Dbx1*$^{+/+}$;*Oprm1*$^{fl/fl}$ control mice, the same
390 concentration had no effect on *f* when μORs were deleted. *, $p<0.05$, Student *t*-test, n=6 for
391 *Dbx1*$^{+/+}$;*Oprm1*$^{fl/fl}$, n=9 for *Dbx1*^{Cre};*Oprm1*$^{fl/fl}$.

392 **Figure 4. Substance P, but not blockade of inhibitory synaptic transmission, blocks the**
393 **depressant effects of DAMGO.**
394 (A) Representative traces of ∫preBötC and ∫XII population activity in 3/1 ACSF control (ctrl) and
395 500 nM SP and 30 nM DAMGO. SP mitigated the effects of DAMGO, and preBötC activity
396 resembled that in control conditions. Scale bar, 10 s.
397 (B) Representative traces of ∫preBötC and ∫XII population activity in 3/1 ACSF control (ctrl) and
398 100 μM picrotoxin/1 μM strychnine and 30 nM DAMGO. The addition of picrotoxin/strychnine
399 following DAMGO application did not recover preBötC *f* to control levels. Scale bar, 10 s.
400 (C) Average normalized *f* of preBötC activity when 30 nM DAMGO was added alone (9/1.5, 3/1)
401 or following application of either 500 nM SP or 100 μM picrotoxin/1 μM strychnine with 30 nM
402 DAMGO. For each experiment, values were normalized to preBötC *f* during baseline 9/1.5 or
403 3/1 ACSF in that experiment. When picrotoxin/strychnine were added with DAMGO, the
404 relative change in *f* did not differ from the normalized *f* when DAMGO was applied alone in
405 either 9/1.5 ACSF or 3/1 ACSF. The normalized *f* when SP was added with DAMGO was
406 significantly higher than all other conditions. *, $p < 0.05$, One-way ANOVA, post-hoc Tukey test,
407 n=6 for 9/1.5, n=7 for 3/1, n=12 for picrotoxin/strychnine, n=6 for SP.
408 (D) Representative traces of ∫preBötC and ∫XII population activity in 3/1 ACSF control (ctrl) and
409 500 nM SP. In control conditions, rhythmic activity consisted of both burstlets and bursts. After
410 SP, *f* was unchanged, but more preBötC bursts were observed. Scale bar, 10 s.

411 (E) Average burstlet fraction and *f* in 3/1 ACSF control condition (ctrl) and 500 nM SP. SP
412 significantly decreased the burstlet fraction, but did not change preBötC *f*. *, $p < 0.05$, Student's
413 t-test, n=13.
414 (F) Representative traces of ∫preBötC and ∫XII population activity in 3/1 ACSF control (ctrl) and
415 100 µM picrotoxin/1 µM strychnine. In control conditions, rhythmic activity consisted of both
416 burstlets and bursts. After picrotoxin/strychnine, *f* was unchanged; however, more preBötC
417 bursts were observed, and XII bursts were larger. Scale bar, 10 s.
418 (G) Average burstlet fraction and *f* in 3/1 ACSF control condition (ctrl) and 100 µM picrotoxin/1
419 µM strychnine. Picrotoxin/strychnine significantly decreased the burstlet fraction, but did not
420 change preBötC *f*. *, $p < 0.05$, Student's t-test, n=13.
421 (H) Model for preBötC rhythm and pattern generation. In the absence of neuromodulation
422 (center), rhythm generation is the alternation between burstlet activity and the silent
423 interburstlet interval (IBI). Pattern generation in the preBötC occurs when burstlet activity
424 reaches a threshold (dashed line) and triggers a burst that is then transmitted to downstream
425 premotoneuronal and motoneuronal populations. Activation of µORs expressed in $Dbx1^+$
426 neurons (left) slows the rhythm by decreasing excitability in $Dbx1^+$ neurons, reducing
427 synchrony, prolonging IBI, and reducing burstlet amplitude. SP (right) may mitigate the effects
428 of µOR activation by increasing *f* or reducing the threshold for burst generation.

429 **Materials and Methods**

430 Experimental procedures were carried out in accordance with the United States Public Health
431 Service and Institute for Laboratory Animal Research Guide for the Care and Use of Laboratory
432 Animals. All protocols were approved by University of California Animal Research Committee
433 and the Rosalind Franklin University of Medicine and Science Institutional Animal Care and Use
434 Committee. Every effort was made to minimize pain and discomfort, as well as the number of
435 animals.

436 *Transgenic mice*

437 *Dbx1*^{Cre} mice (Bielle et al., 2005) were crossed with either *Rosa26*^{tdTomato} (JAX Stock No. 007908)
438 or *Oprm1*$^{fl/fl}$ (Weibel et al., 2013) mouse lines. *Dbx1*^{Cre}*;Rosa26*^{tdTomato} were used to visualize
439 Dbx1^{+} neurons, and *Dbx1*^{Cre}*;Oprm1*$^{fl/fl}$ mice were used to delete µORs selectively in Dbx1^{+}
440 neurons using cre-lox recombination. Animal genotypes were verified via real time polymerase
441 chain reaction using primers specific for the *Oprm1*$^{fl/fl}$ conditional allele or cre recombinase
442 (Pierani et al., 2001; Rose et al., 2009; Weibel et al., 2013) or by direct visualization of
443 fluorescent reporter.

444 *Immunohistochemistry and confocal imaging*

445 *Dbx1*^{Cre}*;Rosa26*^{tdTomato} and *Dbx1*^{Cre}*;Oprm1*$^{fl/fl}$ mice were anesthetized at P0-4 by inhalation of
446 isoflurane. The brainstem was isolated from the pons to the rostral cervical spinal cord, fixed in
447 4% paraformaldehyde, and cryoprotected in 30% sucrose before sectioned at 70mm thickness
448 using CRYOSTAR NX70 (Thermo Scientific). Tissue sections were washed in PBS, and incubated
449 in primary antibody at least overnight, followed by incubation in secondary antibody for 2 hrs at
450 room temperature, and cover-slipped in Vectashield with or without DAPI. Primary antibodies
451 used included rabbit anti-µOR (1:400), goat anti-ChAT (1:400, SCBT); Secondary antibodies were
452 species specific (1:250) and conjugated to Alexa 488, Rhodamine or Cy5 (Invitrogen or Jackson
453 ImmunoResearch). Sections were imaged using confocal laser scanning microscopy. Confocal
454 images were captured on a Zeiss LSM 710 Meta confocal microscope implemented on an
455 upright Axioplan 2 microscope. Zen software was used to capture images. Confocal images

456 were analyzed with ImageJ, and the final figures were composed in Adobe Photoshop and/or
457 Microsoft Powerpoint.

458 *In situ hybridization*

459 As described above, mice were anesthetized at P0-4 by inhalation of isoflurane. The isolated
460 brainstem was rapidly frozen in dry ice and stored at -80°C until sectioning. Transverse sections
461 (14-20 µm) were cut on a cryostat (CryoStar NX70, Thermo Scientific) and mounted on
462 SuperFrost Plus (Fisher Scientific) slides. Slides were processed for fluorescence *in situ*
463 hybridization of three target RNAs simultaneously according to manufacturer protocols for
464 RNAScope® (Advanced Cell Diagnostics). Briefly, fresh frozen tissue samples were postfixed in
465 10% neutral buffered formalin, washed, and dehydrated in sequential concentrations of
466 ethanol (50, 70 and 100%) at RT. Samples were treated with protease IV, then incubated for
467 two hours at 40°C in the presence of target probes to allow for hybridization. The following
468 target probes were used: Mm-Oprm1, Mm-Tac1, and Mm-ChAT. A series of three amplification
469 steps was necessary to provide substrates for target fluorophore labeling (ChAT conjugated to
470 fluorescein (1:1200), Oprm1 to Cy5, (1:1200) and Tac1 to Cy3 (1:1500) (Jackson
471 ImmunoResearch). After labeling, samples were counterstained with DAPI. ProLong® Gold
472 (Invitrogen), was applied to each slide prior to cover slipping. Images were acquired on a
473 confocal laser scanning microscope (LSM710 META, Zeiss). High-resolution z-stack confocal
474 images were taken at 0.3 µm intervals. Cell-by-cell µOR expression profiles were quantified in
475 selected regions of interest (NK1 positive neurons in preBötC) by binning cells with levels of
476 expression, were a dot (>0.60 µm) represents a single RNA transcript. The data was then
477 calculated as a Histo score, using image-based software analysis (FIJI).

478 $$\mathrm{H-score} = \sum_{\substack{bin \\ 0-4}}^{n} (\text{ACD score x percentage of cells per bin})$$

479 *Slice preparation and electrophysiology*

480 Neonatal C57BL/6 or mutant mice (P0-5) of either sex were used for cutting brainstem
481 medullary transverse slices (550-600 µm thick) containing the rhythm-generating preBötC, XII

482 inspiratory motoneurons, and premotoneurons linking these populations (Koizumi et al., 2008;
483 Smith et al., 1991). To obtain slices with the preBötC at the surface, the rostral cut was made
484 above the first set of XII nerve rootlets at the level of the dorsomedial cell column and principal
485 lateral loop of the inferior olive, and the caudal cut captured the obex (Ruangkittisakul et al.,
486 2011). Slice cutting artificial cerebrospinal fluid (ACSF) solution was composed of (in mM): 124
487 NaCl, 3 KCl, 1.5 $CaCl_2$, 1 $MgSO_4$, 25 $NaHCO_3$, 0.5 NaH_2PO_4, and 30 D-glucose, equilibrated with
488 95% O_2 and 5% CO_2, 27°C, pH 7.4. Slices were placed rostral side up in a chamber and perfused
489 at 2-3 ml/min with 28-30°C recording ACSF. Baseline recording ACSF consisted of either the
490 cutting ACSF solution with K^+ raised to 9 mM and Ca^{2+} maintained at 1.5 mM (9/1.5 ACSF) for a
491 robust burst rhythm or the cutting ACSF solution with K^+ maintained at 3 mM and Ca^{2+} lowered
492 to 1 mM (3/1 ACSF) to study burstlets and bursts together (Kam et al., 2013a). In all
493 experiments, slices were allowed to equilibrate for 30 min to ensure that the frequency and
494 magnitude of XII and preBötC population activities reached steady-state. Respiratory activity
495 reflecting suprathreshold action potential firing from populations of neurons was recorded
496 from XII motor nucleus or nerve roots and as population activity directly from the preBötC using
497 suction electrodes (tip size ~50 µm) and an Axiopatch 200A (Molecular Devices), Multiclamp
498 700B (Molecular Devices), and/or a differential AC amplifier (AM systems), filtered at 2–4 kHz,
499 integrated, and digitized at 10 kHz. Integration was performed on custom built Paynter filter
500 with a 20-100 ms time constant. Digitized data were analyzed off-line using custom procedures
501 written for IgorPro (Wavemetrics).

502 *Holographic photostimulation*

503 Holographic photostimulation was performed on a Phasor SLM system (Intelligent Imaging
504 Innovations, Inc.) mounted around an epifluorescence upright microscope (Axioscope; Zeiss).
505 We used a 405 nm diode laser (CUBE 405-100; Coherent) to uncage MNI-glutamate (0.5 mM)
506 and depolarize targeted neurons. An iterative Fourier transform algorithm, implemented in
507 Slidebook 5 (Intelligent Imaging Innovations, Inc.), computed the phase pattern on the SLM
508 corresponding to the desired distribution of light intensity at the focal plane of the objective. A
509 blocker was inserted in the intermediate Fourier plane to block the unmodulated light

510 component (zero order spot) and replicate patterns (Golan et al., 2009). Neurons were targeted
511 by centering 10 um circular spots over the somata of the selected neurons. The laser intensity
512 per spot was set at 1-3 mW, which was previously determined to elicit bursts of action
513 potentials in the targeted neurons without the spread of glutamate to neighboring neurons
514 (Kam et al., 2013b). Each laser stimulation consisted of 5 x 0.8 ms pulses, delivered at 200 Hz. A
515 threshold stimulus was determined as the minimum number of neurons and minimum laser
516 power required to entrain preBötC bursts at slightly faster than the endogenous frequency with
517 a success rate > 80%.

518 *Data analysis and statistics*

519 Semiautomated event detection of respiratory-related activity recorded in XII output or
520 preBötC population recordings was performed using custom procedures written in IgorPro.
521 Multiple criteria, including slope and amplitude thresholds, were used to select events
522 automatically, which were then confirmed visually. Event duration, amplitude, shape, and
523 synchrony between XII and preBötC activity were criteria used to categorize detected events as
524 burstlets, bursts, and doublets. Burstlets were events in preBötC that did not temporally
525 overlap a XII burst. Doublets were distinguished from bursts by their longer duration and the
526 presence of multiple peaks of activity. Two closely spaced bursts were considered a doublet
527 based on the distribution of the period of XII output. A small peak at <2 s in the distribution of
528 periods of XII bursts was usually observed. A Gaussian was fit to this small peak and a threshold
529 time interval was set. Two bursts separated by less than this threshold were considered a
530 doublet. As doublets were in phase with bursts and burstlets, these events were grouped with
531 bursts and not separately analyzed.

532 Rhythmogenic processes were captured by measuring the frequency of preBötC rhythmic
533 activity, which included small amplitude burstlets that were not transmitted to XII motor
534 output, larger amplitude bursts that produced XII bursts, and longer duration doublets that
535 were also transmitted to XII motoneurons. The average frequency was calculated as the mean
536 of the instantaneous frequencies (1/interevent interval) across all preBötC activity (burstlets,
537 bursts, and doublets) in that condition. Pattern generating processes that included the

538 production and transmission of preBötC activity to XII output were characterized by measuring
539 the fraction of preBötC events that were burstlets. The burstlet fraction was calculated as the
540 ratio of the number of burstlets to the total number of rhythmic preBötC events (burstlets,
541 bursts, and doublets). Amplitudes were normalized to the amplitude of the largest burst in the
542 control condition. The latency between laser stimulation and burst initiation was calculated as
543 the time between the start of the next preBötC burst and the beginning of laser stimulation.
544 preBötC activity was used here, rather than XII activity, to isolate the effects of DAMGO on
545 rhythmogenic mechanisms and avoid additional delays or failures due to depression of XII
546 premotoneurons and motoneurons. Successful triggering of a burst by photostimulation was
547 defined as burst detection within 0.5 s of laser stimulation.

548 Data are expressed as mean ± SD. Comparisons between two groups were performed with
549 paired or unpaired Student's *t*-tests. Multiple comparisons were evaluated using parametric
550 one-way or two-way repeated measures ANOVA. Post-hoc Tukey or paired Student's *t*-tests
551 with the Bonferroni-Holm comparison were then used to determine significance for within
552 group comparisons. Statistical significance was set at $p < 0.05$.

553

554 **Supplemental Figure Legends**

555 **Figure S1. μOR, TAC1, and NK1R expression in preBötC.** Related to Figure 3.
556 (A) Confocal image of a medullary brainstem section at the level of the preBötC from a P2 wild
557 type mouse triple processed with RNAScope. Probes for NK1R (green), μOR (magenta), and
558 TAC1 (white) were used, and the tissue was counterstained with DAPI (blue). Scale bar, 20 μm.
559 (B) Higher magnification images of preBötC neurons with (arrows) and without (arrowhead)
560 TAC1 expression. Colocalization of TAC1, NK1R, and μOR puncta was observed in several
561 neurons. Scale bar, 25 μm.

562 **Figure S2. Substance P increases preBötC *f* in *Dbx1^{Cre};Oprm1$^{fl/fl}$* mice.** Related to Figure 4.
563 (A) Representative traces of ∫preBötC and ∫XII population activity from a *Dbx1^{Cre};Oprm1$^{fl/fl}$* slice
564 in control (ctrl, left), 100 nM DAMGO (middle), and 500 nM Substance P (SP, right). Scale bar,
565 10 s.
566 (B) SP (500 nM) significantly increased preBötC *f* on slices from *Dbx1^{Cre};Oprm1$^{fl/fl}$* mice, while
567 DAMGO had no effect *, $p < 0.05$, One-way ANOVA post-hoc Tukey test, n=4.

568 **References**

569 Ballanyi, K., and Ruangkittisakul, A. (2009). Structure-function analysis of rhythmogenic
570 inspiratory pre-Botzinger complex networks in "calibrated" newborn rat brainstem
571 slices. Respir Physiol Neurobiol *168*, 158-178.
572 Bielle, F., Griveau, A., Narboux-Neme, N., Vigneau, S., Sigrist, M., Arber, S., Wassef, M., and
573 Pierani, A. (2005). Multiple origins of Cajal-Retzius cells at the borders of the developing
574 pallium. Nature neuroscience *8*, 1002-1012.
575 Boom, M., Niesters, M., Sarton, E., Aarts, L., Smith, T.W., and Dahan, A. (2012). Non-analgesic
576 effects of opioids: opioid-induced respiratory depression. Current pharmaceutical design
577 *18*, 5994-6004.
578 Bouvier, J., Thoby-Brisson, M., Renier, N., Dubreuil, V., Ericson, J., Champagnat, J., Pierani, A.,
579 Chedotal, A., and Fortin, G. (2010). Hindbrain interneurons and axon guidance signaling
580 critical for breathing. Nature neuroscience *13*, 1066-1074.
581 Davies, J., and Dray, A. (1977). Substance P and opiate receptors. Nature *268*, 351-352.
582 Del Negro, C.A., Kam, K., Hayes, J.A., and Feldman, J.L. (2009). Asymmetric control of inspiratory
583 and expiratory phases by excitability in the respiratory network of neonatal mice in
584 vitro. The Journal of physiology *587*, 1217-1231.
585 Feldman, J.L., and Del Negro, C.A. (2006). Looking for inspiration: new perspectives on
586 respiratory rhythm. Nat Rev Neurosci *7*, 232-242.
587 Feldman, J.L., Del Negro, C.A., and Gray, P.A. (2013). Understanding the rhythm of breathing: so
588 near, yet so far. Annual review of physiology *75*, 423-452.
589 Fukazawa, Y., Maeda, T., Kiguchi, N., Tohya, K., Kimura, M., and Kishioka, S. (2007). Activation of
590 spinal cholecystokinin and neurokinin-1 receptors is associated with the attenuation of
591 intrathecal morphine analgesia following electroacupuncture stimulation in rats. Journal
592 of pharmacological sciences *104*, 159-166.
593 Golan, L., Reutsky, I., Farah, N., and Shoham, S. (2009). Design and characteristics of
594 holographic neural photo-stimulation systems. Journal of neural engineering *6*, 066004.
595 Gray, P.A., Hayes, J.A., Ling, G.Y., Llona, I., Tupal, S., Picardo, M.C., Ross, S.E., Hirata, T., Corbin,
596 J.G., Eugenin, J.*, et al.* (2010). Developmental origin of preBotzinger complex respiratory
597 neurons. The Journal of neuroscience : the official journal of the Society for
598 Neuroscience *30*, 14883-14895.
599 Gray, P.A., Janczewski, W.A., Mellen, N., McCrimmon, D.R., and Feldman, J.L. (2001). Normal
600 breathing requires preBotzinger complex neurokinin-1 receptor-expressing neurons.
601 Nature neuroscience *4*, 927-930.
602 Gray, P.A., Rekling, J.C., Bocchiaro, C.M., and Feldman, J.L. (1999). Modulation of respiratory
603 frequency by peptidergic input to rhythmogenic neurons in the preBotzinger complex.
604 Science *286*, 1566-1568.
605 Hayes, J.A., Kottick, A., Picardo, M.C.D., Halleran, A.D., Smith, R.D., Smith, G.D., Saha, M.S., and
606 Del Negro, C.A. (2017). Transcriptome of neonatal preBotzinger complex neurones in
607 Dbx1 reporter mice. Scientific reports *7*, 8669.
608 Janczewski, W.A., Onimaru, H., Homma, I., and Feldman, J.L. (2002). Opioid-resistant
609 respiratory pathway from the preinspiratory neurones to abdominal muscles: in vivo
610 and in vitro study in the newborn rat. The Journal of physiology *545*, 1017-1026.

611 Janczewski, W.A., Tashima, A., Hsu, P., Cui, Y., and Feldman, J.L. (2013). Role of inhibition in
612 respiratory pattern generation. The Journal of neuroscience : the official journal of the
613 Society for Neuroscience *33*, 5454-5465.
614 Johnson, S.M., Smith, J.C., and Feldman, J.L. (1996). Modulation of respiratory rhythm in vitro:
615 role of Gi/o protein-mediated mechanisms. Journal of applied physiology *80*, 2120-2133.
616 Kam, K., Worrell, J.W., Janczewski, W.A., Cui, Y., and Feldman, J.L. (2013a). Distinct inspiratory
617 rhythm and pattern generating mechanisms in the preBotzinger complex. The Journal of
618 neuroscience : the official journal of the Society for Neuroscience *33*, 9235-9245.
619 Kam, K., Worrell, J.W., Ventalon, C., Emiliani, V., and Feldman, J.L. (2013b). Emergence of
620 population bursts from simultaneous activation of small subsets of preBötzinger
621 complex inspiratory neurons. The Journal of neuroscience : the official journal of the
622 Society for Neuroscience *33*, 3332-3338.
623 Kibaly, C., Xu, C., Cahill, C.M., Evans, C.J., and Law, P.Y. (2019). Non-nociceptive roles of opioids
624 in the CNS: opioids' effects on neurogenesis, learning, memory and affect. Nat Rev
625 Neurosci *20*, 5-18.
626 Koizumi, H., Wilson, C.G., Wong, S., Yamanishi, T., Koshiya, N., and Smith, J.C. (2008). Functional
627 imaging, spatial reconstruction, and biophysical analysis of a respiratory motor circuit
628 isolated in vitro. The Journal of neuroscience : the official journal of the Society for
629 Neuroscience *28*, 2353-2365.
630 Kream, R.M., Kato, T., Shimonaka, H., Marchand, J.E., and Wurm, W.H. (1993). Substance P
631 markedly potentiates the antinociceptive effects of morphine sulfate administered at
632 the spinal level. Proceedings of the National Academy of Sciences of the United States of
633 America *90*, 3564-3568.
634 Lalley, P.M., Pilowsky, P.M., Forster, H.V., and Zuperku, E.J. (2014). CrossTalk opposing view:
635 The pre-Botzinger complex is not essential for respiratory depression following systemic
636 administration of opioid analgesics. The Journal of physiology *592*, 1163-1166.
637 Le Merrer, J., Becker, J.A., Befort, K., and Kieffer, B.L. (2009). Reward processing by the opioid
638 system in the brain. Physiological reviews *89*, 1379-1412.
639 Lu, B., Su, Y., Das, S., Liu, J., Xia, J., and Ren, D. (2007). The neuronal channel NALCN contributes
640 resting sodium permeability and is required for normal respiratory rhythm. Cell *129*,
641 371-383.
642 Mansour, A., Khachaturian, H., Lewis, M.E., Akil, H., and Watson, S.J. (1988). Anatomy of CNS
643 opioid receptors. Trends in neurosciences *11*, 308-314.
644 Manzke, T., Guenther, U., Ponimaskin, E.G., Haller, M., Dutschmann, M., Schwarzacher, S., and
645 Richter, D.W. (2003). 5-HT4(a) receptors avert opioid-induced breathing depression
646 without loss of analgesia. Science *301*, 226-229.
647 Montandon, G., and Horner, R. (2014). CrossTalk proposal: The preBotzinger complex is
648 essential for the respiratory depression following systemic administration of opioid
649 analgesics. The Journal of physiology *592*, 1159-1162.
650 Montandon, G., Qin, W., Liu, H., Ren, J., Greer, J.J., and Horner, R.L. (2011). PreBotzinger
651 complex neurokinin-1 receptor-expressing neurons mediate opioid-induced respiratory
652 depression. The Journal of neuroscience : the official journal of the Society for
653 Neuroscience *31*, 1292-1301.

654 Montandon, G., Ren, J., Victoria, N.C., Liu, H., Wickman, K., Greer, J.J., and Horner, R.L. (2016).
655 G-protein-gated Inwardly Rectifying Potassium Channels Modulate Respiratory
656 Depression by Opioids. Anesthesiology *124*, 641-650.
657 Phillips, R.S., Cleary, D.R., Nalwalk, J.W., Arttamangkul, S., Hough, L.B., and Heinricher, M.M.
658 (2012). Pain-facilitating medullary neurons contribute to opioid-induced respiratory
659 depression. Journal of neurophysiology *108*, 2393-2404.
660 Picardo, M.C.D., Sugimura, Y.K., Dorst, K.E., Kallurkar, P.S., Akins, V.T., Ma, X., Teruyama, R.,
661 Guinamard, R., Kam, K., Saha, M.S., *et al.* (2019). Trpm4 ion channels in pre-Botzinger
662 complex interneurons are essential for breathing motor pattern but not rhythm. PLoS
663 biology *17*, e2006094.
664 Pierani, A., Moran-Rivard, L., Sunshine, M.J., Littman, D.R., Goulding, M., and Jessell, T.M.
665 (2001). Control of interneuron fate in the developing spinal cord by the progenitor
666 homeodomain protein Dbx1. Neuron *29*, 367-384.
667 Pokorski, M., and Lahiri, S. (1981). Effects of naloxone on carotid body chemoreception and
668 ventilation in the cat. Journal of applied physiology: respiratory, environmental and
669 exercise physiology *51*, 1533-1538.
670 Prkic, I., Mustapic, S., Radocaj, T., Stucke, A.G., Stuth, E.A., Hopp, F.A., Dean, C., and Zuperku,
671 E.J. (2012). Pontine mu-opioid receptors mediate bradypnea caused by intravenous
672 remifentanil infusions at clinically relevant concentrations in dogs. Journal of
673 neurophysiology *108*, 2430-2441.
674 Ren, J., and Greer, J.J. (2006). Modulation of respiratory rhythmogenesis by chloride-mediated
675 conductances during the perinatal period. The Journal of neuroscience : the official
676 journal of the Society for Neuroscience *26*, 3721-3730.
677 Rose, M.F., Ren, J., Ahmad, K.A., Chao, H.T., Klisch, T.J., Flora, A., Greer, J.J., and Zoghbi, H.Y.
678 (2009). Math1 is essential for the development of hindbrain neurons critical for
679 perinatal breathing. Neuron *64*, 341-354.
680 Ruangkittisakul, A., Panaitescu, B., and Ballanyi, K. (2011). K(+) and Ca(2)(+) dependence of
681 inspiratory-related rhythm in novel "calibrated" mouse brainstem slices. Respir Physiol
682 Neurobiol *175*, 37-48.
683 Schmidt, Y., Gaveriaux-Ruff, C., and Machelska, H. (2013). mu-Opioid receptor antibody reveals
684 tissue-dependent specific staining and increased neuronal mu-receptor
685 immunoreactivity at the injured nerve trunk in mice. PloS one *8*, e79099.
686 Shao, X.M., and Feldman, J.L. (1997). Respiratory rhythm generation and synaptic inhibition of
687 expiratory neurons in pre-Botzinger complex: differential roles of glycinergic and
688 GABAergic neural transmission. Journal of neurophysiology *77*, 1853-1860.
689 Smith, J.C., Ellenberger, H.H., Ballanyi, K., Richter, D.W., and Feldman, J.L. (1991). Pre-Botzinger
690 complex: a brainstem region that may generate respiratory rhythm in mammals. Science
691 *254*, 726-729.
692 Stucke, A.G., Miller, J.R., Prkic, I., Zuperku, E.J., Hopp, F.A., and Stuth, E.A. (2015). Opioid-
693 induced Respiratory Depression Is Only Partially Mediated by the preBotzinger Complex
694 in Young and Adult Rabbits In Vivo. Anesthesiology *122*, 1288-1298.
695 Tan, W., Pagliardini, S., Yang, P., Janczewski, W.A., and Feldman, J.L. (2010). Projections of
696 preBotzinger complex neurons in adult rats. The Journal of comparative neurology *518*,
697 1862-1878.

698 van der Schier, R., Roozekrans, M., van Velzen, M., Dahan, A., and Niesters, M. (2014). Opioid-
699 induced respiratory depression: reversal by non-opioid drugs. F1000prime reports *6*, 79.
700 Wang, X., Hayes, J.A., Revill, A.L., Song, H., Kottick, A., Vann, N.C., LaMar, M.D., Picardo, M.C.,
701 Akins, V.T., Funk, G.D.*, et al.* (2014). Laser ablation of Dbx1 neurons in the pre-Botzinger
702 complex stops inspiratory rhythm and impairs output in neonatal mice. eLife *3*, e03427.
703 Weibel, R., Reiss, D., Karchewski, L., Gardon, O., Matifas, A., Filliol, D., Becker, J.A., Wood, J.N.,
704 Kieffer, B.L., and Gaveriaux-Ruff, C. (2013). Mu opioid receptors on primary afferent
705 nav1.8 neurons contribute to opiate-induced analgesia: insight from conditional
706 knockout mice. PloS one *8*, e74706.
707 Williams, J.T., Christie, M.J., and Manzoni, O. (2001). Cellular and synaptic adaptations
708 mediating opioid dependence. Physiological reviews *81*, 299-343.
709 Yeh, S.Y., Huang, W.H., Wang, W., Ward, C.S., Chao, E.S., Wu, Z., Tang, B., Tang, J., Sun, J.J.,
710 Esther van der Heijden, M.*, et al.* (2017). Respiratory Network Stability and Modulatory
711 Response to Substance P Require Nalcn. Neuron *94*, 294-303 e294.
712 Zhang, Z., Xu, F., Zhang, C., and Liang, X. (2007). Activation of opioid mu receptors in caudal
713 medullary raphe region inhibits the ventilatory response to hypercapnia in anesthetized
714 rats. Anesthesiology *107*, 288-297.
715 Zhang, Z., Zhuang, J., Zhang, C., and Xu, F. (2011). Activation of opioid mu-receptors in the
716 commissural subdivision of the nucleus tractus solitarius abolishes the ventilatory
717 response to hypoxia in anesthetized rats. Anesthesiology *115*, 353-363.
718
719

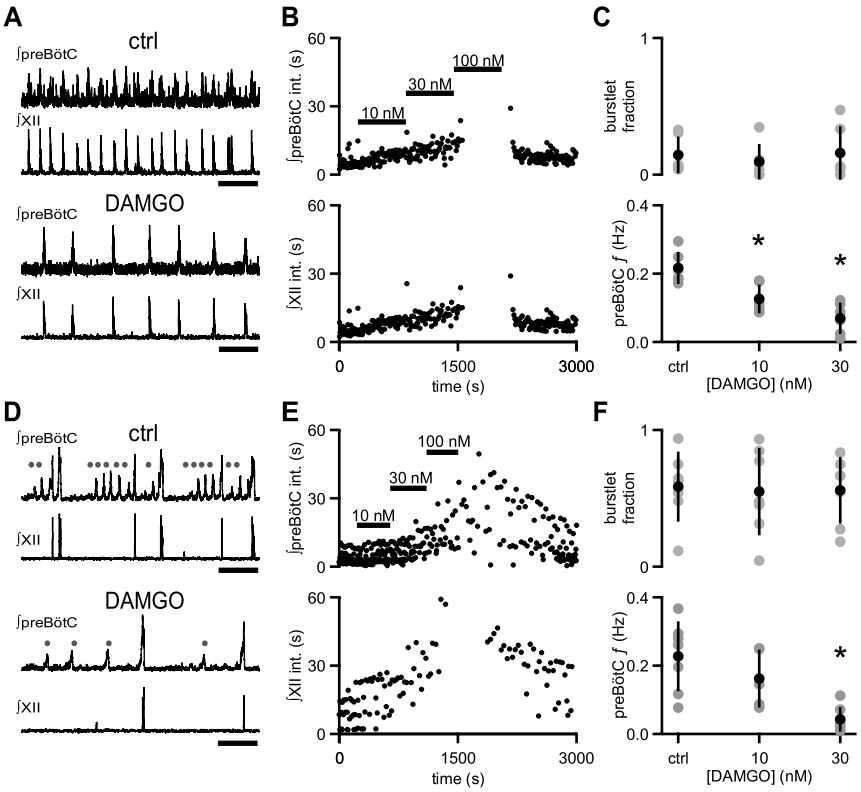
A
ctrl
∫preBötC
∫XII
DAMGO
∫preBötC
∫XII
B
∫preBötC int. (s)
10 nM
30 nM
100 nM
∫XII int. (s)
time (s)
C
burstlet fraction
preBötC f (Hz)
[DAMGO] (nM)
ctrl
D
ctrl
∫preBötC
∫XII
DAMGO
∫preBötC
∫XII
E
∫preBötC int. (s)
10 nM
30 nM
100 nM
∫XII int. (s)
time (s)
F
burstlet fraction
preBötC f (Hz)
[DAMGO] (nM)
ctrl

Figure 1

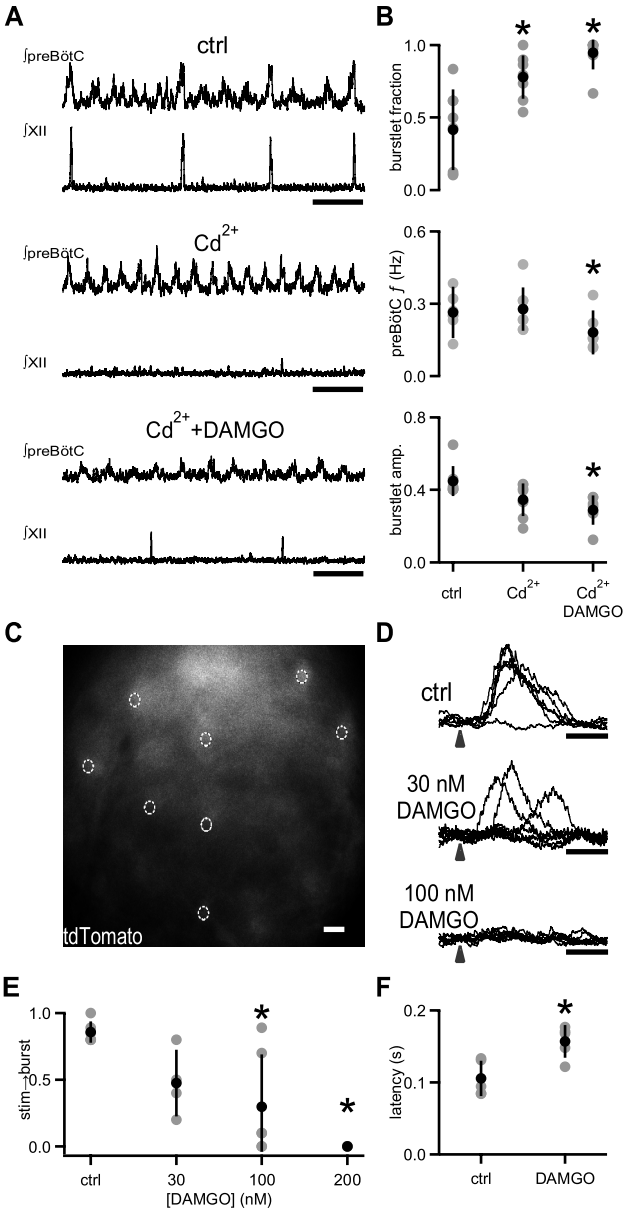
A
ctrl
∫preBötC
∫XII
Cd2+
Cd2+ +DAMGO
B
burstlet fraction
preBötC f (Hz)
burstlet amp.
ctrl
Cd2+
Cd2+ DAMGO
C
tdTomato
D
ctrl
30 nM DAMGO
100 nM DAMGO
E
stim→burst
[DAMGO] (nM)
F
latency (s)
DAMGO

Figure 2

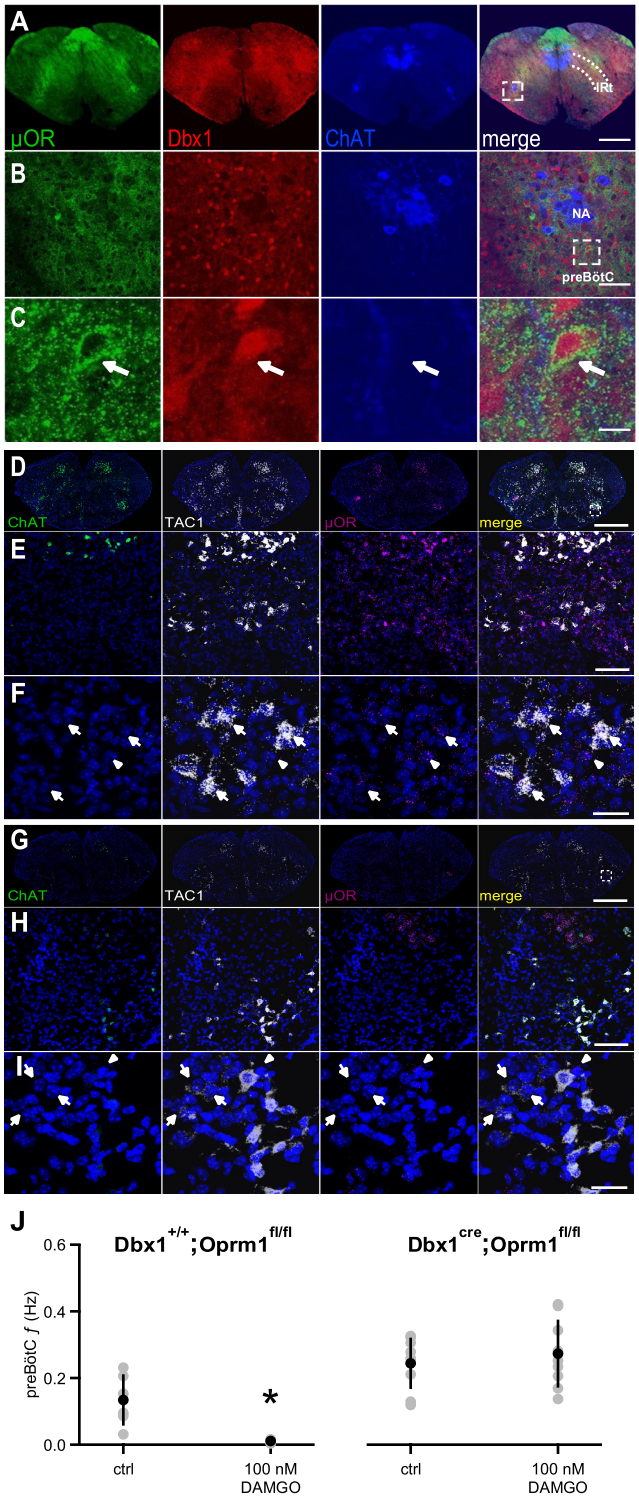
A
μOR
Dbx1
ChAT
merge
Rt
B
NA
preBötC
C
D
ChAT
TAC1
μOR
merge
E
F
G
ChAT
TAC1
μOR
merge
H
I
J
Dbx1+/+;Oprm1fl/fl
Dbx1cre;Oprm1fl/fl
preBötC f (Hz)
0.6
0.4
0.2
0.0
*
ctrl
100 nM DAMGO
ctrl
100 nM DAMGO

Figure 3

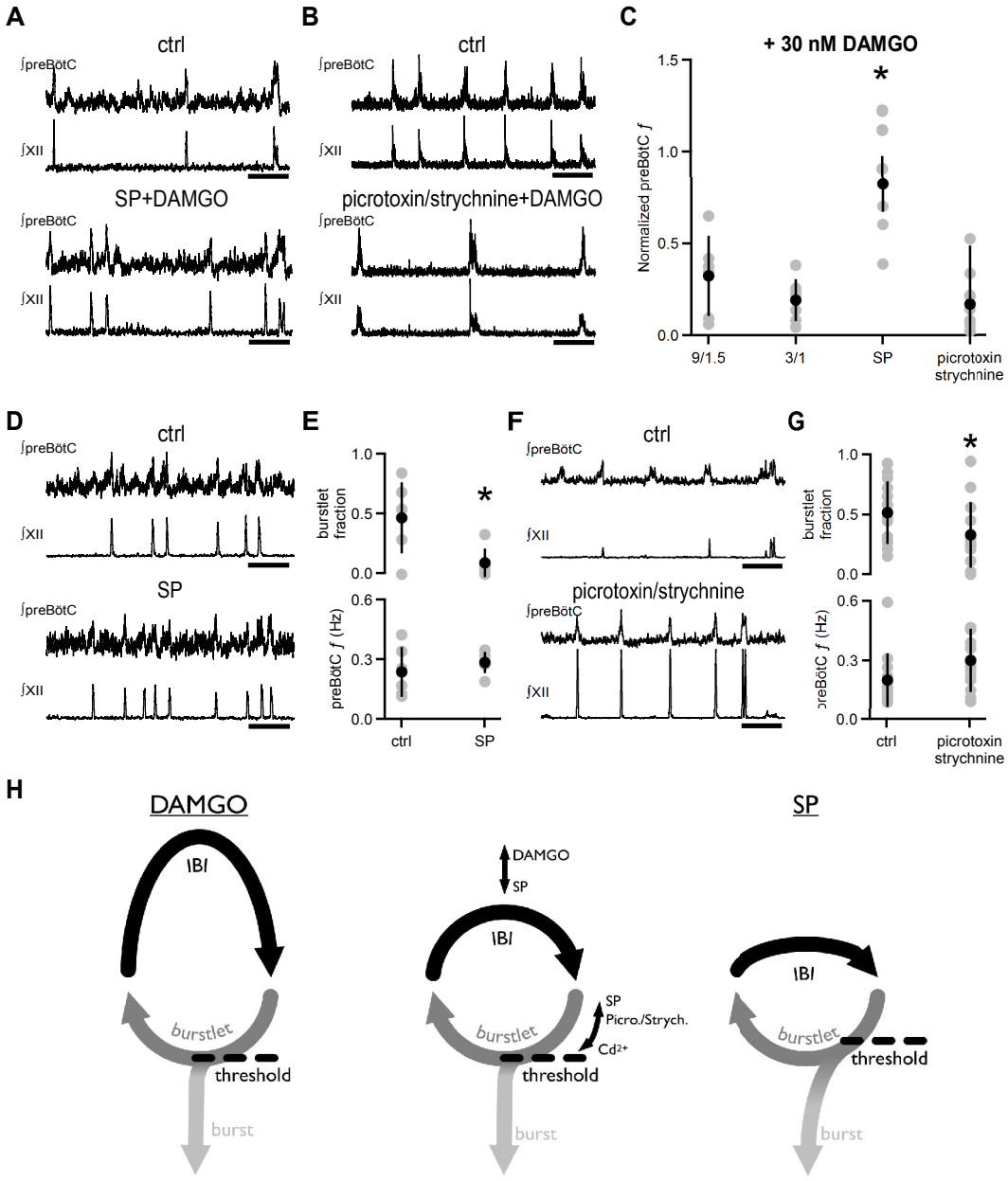
A
ctrl
∫preBötC
∫XII
SP+DAMGO
∫preBötC
∫XII
B
ctrl
∫preBötC
∫XII
picrotoxin/strychnine+DAMGO
∫preBötC
∫XII
C
+ 30 nM DAMGO
Normalized preBötC f
1.5
1.0
0.5
0.0
*
9/1.5
3/1
SP
picrotoxin
strychnine
D
ctrl
∫preBötC
∫XII
SP
∫preBötC
∫XII
E
burstlet fraction
1.0
0.5
0.0
*
preBötC f (Hz)
0.6
0.3
0.0
ctrl
SP
F
ctrl
∫preBötC
∫XII
picrotoxin/strychnine
∫preBötC
∫XII
G
burstlet fraction
1.0
0.5
0.0
*
preBötC f (Hz)
0.6
0.3
0.0
ctrl
picrotoxin
strychnine
H
DAMGO
IBI
burstlet
threshold
burst
DAMGO
SP
IBI
SP
Picro./Strych.
Cd2+
burstlet
threshold
burst
SP
IBI
burstlet
threshold
burst

Figure 4